Tracing the evolution of morphology and mixing state of soot particles along with the movement of an Asian dust storm

Liang Xu[1], Satoshi Fukushima[2], Sophie Sobanska[3], Kotaro Murata[2], Ayumi Naganuma[2], Lei Liu[1],

Yuanyuan Wang[1], Hongya Niu[4], Zongbo Shi[5], Tomoko Kojima[6], Daizhou Zhang[2], Weijun Li[1,*]

[1]Department of Atmospheric Sciences, School of Earth Sciences, Zhejiang University, Hangzhou

310027, China

[2]Faculty of Environmental and Symbiotic Sciences, Prefectural University of Kumamoto,

Kumamoto 862-8502, Japan

[3]Institute of Molecular Sciences, UMR CNRS 5255, University of Bordeaux, 351 cours de la

libération, 33405 Talence, France

[4]Key Laboratory of Resource Exploration Research of Hebei Province, Hebei University of

Engineering, Handan 056038, Hebei, China

[5]School of Geography, Earth and Environmental Sciences, University of Birmingham, UK

[6]Department Earth and Environmental Science, Faculty of Advanced Science and Technology,

Kumamoto University, Kumamoto 860-8555, Japan

*Corresponding author: W. Li (liweijun@zju.edu.cn)

Department of Atmospheric Sciences, School of Earth Sciences, Zhejiang University, Hangzhou

310027, China

Abstract

Tracing the aging progress of soot particles during transport is highly challenging. An Asian dust event could provide an ideal opportunity to trace the continuous aging progress of long-range transported soot particles. Here, we collected individual aerosol particles at an inland urban site (T1) and a coastal urban site (T2) in China and a coastal site (T3) in southwestern Japan during an Asian dust event. Microscopic analysis showed that the number fraction of soot-bearing particles was 19% and 16% at T1 and T2 in China but surprisingly increased to 56% at T3 in Japan. The dominant fresh soot (71%) at T1 became partially embedded (68%) at T2 and fully embedded (84%) at T3. These results indicated that the tiny soot particles had lower deposition than other aerosol types and became more aged during the transport from T1 to T3. We quantified soot morphology using the fractal dimension and found the trend from 1.65 at T1, 1.84 at T2, and to 1.91 at T3. Furthermore, we found that the morphology compression of the soot aggregations was associated with secondary coating thickness and relative humidity. A unique mixing structure that multi-soot particles scattered in organic coatings instead of sulfate core in individual core-shell particles was observed at T3 after the crossing of the East China Sea. The study well understands important constraints of the soot morphological effects and provides possible aging scale along with their transport pathway. These new findings will be helpful to improve optical calculation and regional climate modeling of soot particles during their transport in the atmosphere.

1. Introduction

Soot (i.e., black carbon (BC)) is a type of carbonaceous material with graphitic structures emitted from the incomplete combustion of fossil fuels and biomass. Soot particles exhibit a chain-like aggregation morphology with a diameter of 10 nm to 100 nm (Buseck et al., 2014). Because of its strong capacity to absorb solar radiation, soot is considered the second greatest contributor to global warming after carbon dioxide (IPCC., 2013;Bond et al., 2013). Soot is an important particulate pollutant in fine particles (i.e., $PM_{2.5}$) in urban polluted air, which adversely affects the respiratory health of citizens and induces generally unwanted heating in the planetary boundary layer (West et al., 2016;Ding et al., 2016).

Fresh soot particles are hydrophobic but are converted into a hydrophilic state following their aging through physical and chemical processes (Li et al., 2016b;Riemer et al., 2010;Perring et al., 2017). Aged soot particles containing secondary coating aerosols (e.g., ammonium sulfate, ammonium nitrate, and organic matter) can be activated as cloud condensation nuclei (CCN) (Zhang et al., 2008;Wang et al., 2010;Ding et al., 2019;Shiraiwa et al., 2007;Lee et al., 2019). These coatings can significantly change the optical scattering and absorption capacity of soot particles (Liu et al., 2017;Moffet and Prather, 2009;Matsui et al., 2018;He et al., 2015;Zhang et al., 2018a). Numerical model simulations have estimated that light absorption by internally mixed soot is enhanced by a factor of 2 over externally mixed soot (Jacobson, 2001). In contrast, Cappa et al. (2012) reported in situ observations of soot absorption enhancement of only 6% in ambient air. This discrepancy between simulation and

67 observation could be attributed to the complex mixing structure and various

68 morphologies of soot particles in the air (Adachi et al., 2016;Li et al., 2016a;Wu et al.,

69 2018).

70   In aged air masses, soot particles tend to be internally mixed with secondary

71 aerosols such as sulfates, nitrates, and secondary organic matter (Li et al., 2016b).

72 Especially in the East Asian region, one of the most polluted areas in the world, soot is

73 internally mixed with secondary aerosols in polluted urban, rural, and remote air

74 (Adachi et al., 2016;Zhang et al., 2013;Yuan et al., 2019;Zhang et al., 2018b). However,

75 most of these studies have focused on the aging and mixing state of soot particles at one

76 or multiple isolated sites. These results have not traced the detailed aging processes

77 (e.g., morphology and mixing structure) from fresh to aged soot particles during their

78 transport.

79   Although great progress has been made in the field of soot aging, it is highly

80 challenging to trace the aging processes of soot particles during transport. Asian dust

81 storms carry both dust and anthropogenic aerosols across East Asia into the North

82 Pacific Ocean (Li et al., 2014;Geng et al., 2014;Zhang et al., 2005). This presents an

83 ideal environment to study the aging processes of soot particles during long-range

84 transport. Compared to previous publications, the present study quantified the variation

85 in mixing structures and fractal dimension of soot particles and further explored how

86 shape of soot particles changed following the dust storm movement from East China to

87 Japan.

88   Using transmission electron microscopy (TEM), we investigated the morphology,

89   mixing structure, relative abundance, and size distribution of individual soot particles.

90   Furthermore, we evaluated the morphological differences of individual soot particles at

91   three sampling sites. Finally, a conceptual model was proposed to better understand the

92   aging processes of long-rang transported soot particles.

93   **2. Experimental methods**

94   **2.1 Aerosol sampling**

95   Three sampling sites were chosen for aerosol collections: an inland urban site in

96   Jinan city (T1, 36.67°N 117.06°E), China, a coastal urban site in Qingdao city (T2,

97   36.10°N 120.46°E), China, and a coastal rural site at Amakusa (T3, 32.30°N 130.00°E)

98   in southwestern Japan (Figure 1). A dust storm outbreak was observed in East Asia.

99   Detailed information about this dust storm will be discussed in Section 3.1. We

100   collected aerosol particles during dust transport from 18 to 19 March 2014 at the three

101   sampling sites (Figure S1-S5). In total, seven dust samples were collected within 30

102   hours after the dust storm arrival. The details about the sampling dates, times,

103   meteorological conditions, and PM (particulate matter) concentrations for the samples

104   are listed in Table S1.

105   A DKL-2 sampler (Genstar Electronic Technology, China) was used to collect

106   individual aerosol particles on copper TEM grids covered by carbon film (carbon type-

107   B, 300-mesh copper; Tianld Co., China) with an air flow of 1.0 L/min. A single-stage

108   impactor with a 0.5 mm diameter jet nozzle was installed on the sampler. This impactor

109   has a collection efficiency of 100% at an aerodynamic diameter of 0.5 μm with an

110   assumed particle density of 2 g/cm^3. The sampling duration varied from 1 min to 2 min

111 according to the visibility, PM concentration, and particle distribution on the substrate.

112 All samples were placed in sealed, dry plastic capsules and stored in a desiccator at

113 25 °C and 20 ± 3% relative humidity (RH) for further analysis.

114 **2.2 Electron microscopic analyses**

115   A JEOL JEM-2100 transmission electron microscopy (TEM) operated at 200 kV

116 was used to analyze individual particles. Elemental composition was determined

117 semiquantitatively by using an energy-dispersive X-ray spectrometer (EDS) (Oxford

118 Instruments, UK) that can detect elements heavier than carbon ($Z \geq 6$). The distribution

119 of aerosol particles on TEM grids was not uniform, with coarser particles occurring

120 near the center and finer particles occurring on the periphery (Xu et al., 2019). Therefore,

121 to ensure that the analyzed particles were representative of the entire size range, three

122 areas were chosen from the center to the periphery of the sampling spot on each grid.

123 iTEM software (Olympus Soft Imaging Solutions GmbH, Germany) was used to

124 analyze the TEM images and obtain the projected area, perimeter, shape factor, and

125 equivalent circle diameter (ECD) of individual aerosol particles. In total, we analyzed

126 412, 486, and 887 aerosol particles for T1, T2, and T3 site, respectively.

127 **2.3 AFM analysis**

128   Atomic force microscopy (AFM) is an analytical method used for studying the

129 surface structure of solid materials. AFM (Dimension Icon, Germany) can determine

130 the three-dimensional morphology of particles in tapping mode. The AFM settings

131 consisted of imaging forces between 1 and 1.5 nN, scanning rates between 0.5 and 0.8

132 Hz, and a scanning range of 10 μm with a resolution of 512 pixels per length. The

133   bearing areas (A) and bearing volumes (V) of the particles were directly obtained from

134   NanoScope Analysis software. Their equivalent circle diameters (ECDs) and equivalent

135   volume diameters (EVDs) were calculated according to the formulas described by Chi

136   et al. (2015).

137   The correlations of ECDs and EVDs are shown in Figure S6 in the Supporting

138   Information. Therefore, the ECD of individual aerosol particles measured from the

139   iTEM software can be further converted into an EVD based on this correlation.

140   **2.4 Air mass backward trajectories**

141   Forty-eight hour backward trajectories were calculated for the three sites using the

142   NOAA HYSPLIT (Hybrid Single Particle Lagrangian Integrated Trajectory) trajectory

143   model (Stein et al., 2015). We selected an altitude of 1500 m as the end point in each

144   backward trajectory.

145   We measured the actual duration from the Beijing-Tianjin-Hebei (BTH) area to T1

146   and T2 according to the backward trajectories in Figure 1. It was approximately 12

147   hours between BTH and T1 and 15 hours between BTH and T2. The interval between

148   T1 and T2 was three hours. The duration between the air mass leaving T2 and reaching

149   T3 was approximately 30 hours.

150   **2.5 Morphological analysis of soot particles**

151   The fractal dimension (D_f) calculated by the scaling law is used to characterize the

152   morphology of soot particles (Koeylue et al., 1995).

153   $$N = k_g \left(\frac{2R_g}{d_p} \right)^{D_f} \tag{1}$$

154   where N is the total number of soot monomers, R_g is the radius of gyration of the soot

155   particle, d_p is the diameter of soot monomer, k_g is the fractal prefactor, and D_f is the

156   mass fractal dimension of an individual soot particle.

157   D_f and k_g in Equation 1 are estimated from a power law fit of a scatter plot of N

158   versus the values of $2R_g/d_p$. N can also be calculated by Equation 2.

159
$$N=k_a \left(\frac{A_a}{A_p}\right)^{\alpha} \tag{2}$$

160   where A_a is the projected area of the soot particle, A_p is the mean projected area of the

161   soot monomer, k_a is a constant, and α is an empirical projected area exponent.

162   The values of α and k_a in Equation 2 depend on the overlap parameter (δ) calculated

163   using Equation 3. Then δ can be used to obtain α and k_a based on Fig. 6. in Oh and

164   Sorensen (1997).

165
$$\delta=\frac{2a}{l} \tag{3}$$

166   where a is the soot monomer radius and l is the monomer spacing.

167   The radius of gyration of the soot particle R_g is obtained by the simple

168   correlation in Equation 4 developed by Brasil et al. (1999)

169
$$L_{max}/(2R_g)=1.50 \pm 0.05 \tag{4}$$

170   where L_{max} is the maximum length of the soot particle.

171   The values of d_p, A_a, A_p, a, l, and L_{max} can be directly obtained from TEM images.

172   In addition to D_f, we also used the shape factor (SF) to further quantify the

173   morphological differences of soot particles. The shape factor is defined as the ratio of

174   the actual area of a particle to the area of a circle with the same perimeter (Equation 5).

175   A shape factor of 1 (the maximum value) indicates a perfectly round particle.

176
$$SF=\frac{4\pi S}{P^2} \tag{5}$$

177   where S is the area of a soot particle and P is the perimeter of a soot particle.

178   **3. Results and discussion**

179   **3.1 The Asian dust storm event**

180   Figure 2 displays variations in PM_{10} and $PM_{2.5}$ concentrations before, during, and

181   after the dust storm event at the Jinan, Qingdao, and Amakusa sampling sites. The dust

182   storm air mass started to influence T1 at approximately 06:00 on 03/17 (Universal Time

183   Coordinated, UTC). The concentration of PM_{10} at T1 increased rapidly to a maximum

184   value of 834 $\mu g/m^3$. The air mass reached T2 at 09:00 on 03/17, and the highest PM_{10}

185   concentration was recorded at 721 $\mu g/m^3$. After the arrival of a cold front at T2, the air

186   mass continued moving approximately 1000 km to T3 at 02:00 on 03/18. The

187   concentration of PM_{10} reached 87 $\mu g/m^3$ at T3 (Figure 2). During this study, the

188   meteorological data (e.g., temperature and air pressure) measured at the three sampling

189   sites also confirm the arrival time of the dust storm (Figures S3-S5). All seven dust

190   samples were collected after the arrival of the dust storm, thus confirming the sampling

191   of the same dust storm event (Figures 2 and S2).

192   Figure 1 indicates that all the air masses during the dust storm event originated

193   from Mongolia, moving southeastward via the BTH area, reaching T1 and T2. The BTH,

194   as the largest city cluster in China, contains one of the largest anthropogenic emission

195   sources (e.g., heavy industries, coal-fired power plants, and vehicles) in the world (Li

196   et al., 2016b). The transport duration from the BTH to T1 and T2 was about 12 hours

197   and 15 hours, respectively. Thus, we estimated that the interval between T1 and T2 was

198   three hours. After passing over T1 and T2, the air masses kept moving southeastward

199   to Japan. The estimated interval between T2 and T3 was 30 hours. The ground PM and

200   meteorological measurements at the three sampling sites (Figure 2 and S3-S5) coupled

201 with air mass back trajectories (Figure 1) and a dust storm simulation in East Asia

202 (Figure S1) together verified that the dust storm event, under the force of a strong cold

203 front, transported across the large BTH city cluster to the downwind area. Therefore,

204 this dust storm movement provides a unique opportunity to study particles in the same

205 air mass and thus trace physical and chemical changes in aerosol particles.

206 **3.2 Classification and mixing state of soot-bearing particles**

207   Soot particles with a typical chain-like structure can be easily distinguished from

208 other aerosol components (e.g., sulfate, organic, metal, and mineral particles) by their

209 morphology. TEM observation is a convenient way to determine whether soot is

210 associated with other aerosol components (Li et al., 2016b;Laskin et al., 2019). During

211 the dust storm period, 56% of the analyzed particles within a size range of 50 nm to 2.4

212 μm included soot particles at T3, approximately three times higher than those at T1

213 (19%) and T2 (16%). This high percentage of internally mixed soot particles was also

214 shown by Ueda et al. (2016) in an Asian outflow at Noto Peninsula, Japan, based on

215 single-particle soot photometer (SP2) analyses. Our results show that the dust storm

216 event not only carried large amounts of dust particles from the Gobi Desert in

217 northwestern China but that this dust-laden air mass also incorporated many soot

218 particles from polluted East Asia (Figure 2 and Figure 3a-d). This is consistent with Pan

219 et al. (2015), who showed that dust storms in East Asia contain and transport

220 anthropogenic pollutants from urban areas.

221   Based on the mixing structures between soot and sulfate on the substrates, three

222 groups of soot particles were defined in this study: fresh, partially embedded and fully

223 embedded (Figure 3).

224   *Fresh soot*. The soot particles were not obviously mixed with secondary aerosol

225 components (Figure 3a). Although surfaces of the fresh soot particles could contain

226 minor organic matter, the organic film was insufficient to change soot morphology and

227 optical properties (Buseck et al., 2014).

228 *Partially embedded soot*. Part of the soot particle was coated by secondary aerosols

229 (Figure 3b). Most of partially embedded soot particles include one soot core, only ~ 10%

230 of them contain two soot cores (Figure S7).

231 *Fully embedded soot*. The entire soot particle was encapsulated by secondary

232 aerosols (Figure 3c). It should be noted that some soot particles were only embedded in

233 the organic coating instead of the sulfur-rich core (Figure 3d).

234 TEM images show that the fully embedded soot particles with a clear rim on the

235 substrate displayed a droplet-like shape (Figure 3c-d), suggesting that these secondary

236 particles were in an aqueous phase in ambient air (Li et al., 2016b).

237 Based on the three mixing structures of soot particles, we further obtained their

238 relative abundance at the three sampling sites (Figure 4). Seventy-one percent of soot-

239 bearing particles were fresh at T1, decreasing to 10% at T2. In contrast, partially

240 embedded soot increased from 14% at T1 to 68% at T2 when the cold front moved from

241 T1 to T2. It should be noted that fresh soot disappeared at T3 after crossing the East

242 China Sea, and the fully embedded soot dominated soot-bearing particles (84%).

243 Following the dust storm movement, we found that the number fraction of total

244 soot-bearing particles increased to 56% among all the analyzed particles from T1 to T3,

245 suggesting that soot particles had lower deposition than other aerosol types in the cold

246 front. Indeed, soot particles normally have smaller sizes and densities than mineral dust,

247 metal, sulfate, and nitrate particles (Peng et al., 2017), suggesting that soot particles can

248 be transported over longer distances during Asian dust storms. Moreover, the number

249 fraction increase of soot-bearing particles also could be attributed to the increase of

250 mixing state index (the metric to quantify the population mixing state, ranging from 0

251 for a completely external mixture to 1 for a completely internal mixture) as aging during

252 transport (Riemer and West, 2013;Healy et al., 2014).

253 **3.3 Quantifying the morphology of soot particles**

254   The fractal dimension (D_f) of soot particles is a key parameter used to reflect soot

255 morphological structure; e.g., compact soot particles usually have larger D_f than lacy

256 aggregates (China et al., 2015;Wang et al., 2017;China et al., 2013). Therefore, D_f can

257 be used to understand soot aging processes in the atmosphere. Figure 5 shows that the

258 D_f sequence of soot particles is T1 (1.65) < T2 (1.84) < T3 (1.91). The D_f of soot

259 particles at T1 (1.65) is much closer to the values of soot emitted from sources, such as

260 the D_f from biomass burning in the range of 1.68−1.74 (Chakrabarty et al., 2006) and

261 the D_f from diesel burning in the range of 1.56−1.68 (Wentzel et al., 2003). The D_f of

262 soot particles at T3 (1.96 for partially embedded soot and 1.88 for fully embedded soot,

263 Figure S8) is close to that of aged soot (1.81-1.90) in remote marine air (China et al.,

264 2015) and polluted air in North China (Wang et al., 2017).

265   At the three sampling sites, the highest D_f value at T3 suggests a more compacted

266 structure of the soot particles. Moreover, we obtained the shape factors of soot particles

267 at the three sampling sites to indicate the compactness of soot particle. The average

268 shape factor of soot particles at T3 was 0.73, much higher than 0.34 at T1 and 0.54 at

269 T2 (Figure 6a). These two parameters show that the soot morphology became more

270 compact and had a rounder shape following the dust storm movement.

3.4 Soot-bearing particle size growth following soot aging

272 The average ratio (D_p/D_{core}) of the diameter of the internally mixed particle (D_p) to

273 its corresponding soot core (D_{core}) during the dust storm period was 1.42 at T1, 1.78 at

274 T2, and 2.49 at T3 (Figure 6b). Size distribution of the soot core indicates a small

275 difference between T1, T2, and T3 during the dust storm period (peak at 200-250 nm,

276 Figure S9). Thus, the D_p/D_{core} increase from T1 to T3 is attributed to the increased

277 coating thickness. The D_p/D_{core} values in this study are much higher than the reported

278 values in fresh emissions (e.g., average value 1.24 for fossil fuel (Sahu et al., 2012))

279 but close to ~2.0 in aged aerosols in background and polluted air (Dahlkötter et al.,

280 2014;Raatikainen et al., 2015;Metcalf et al., 2012). Recently, Peng et al. (2017) reported

281 a high growth rate in urban Beijing and a derived average D_p/D_{core} value of 1.97 (1.34-

282 2.61). The D_p/D_{core} value in urban Beijing air is much higher than our reported values

283 of 1.42-1.78 at T1 and T2 during the dust storm period. This is understandable

284 considering the weak secondary aerosol formation in the dust storm in the continental

285 air as a result of acidic gases being scavenged by the large amounts of mineral dust

286 particles (Li et al., 2016b).

287 Based on the air mass backward trajectories, we can infer that it took approximately

288 three hours for the cold front to move between T1 and T2 and 30 hours from T2 to T3

289 (Figure 1). Here, we calculated the coating volume of aged soot particles based on the

290 values of D_p and D_{core} of individual particles and found a 152% increase in the coating

291 volume from T1 to T2 and a 609% increase from T2 to T3.

3.5 Aging mechanism of soot particles

293 We noticed that the partially embedded soot particles significantly increased from

13

294   14% at T1 to 68% at T2 (Figure 4), indicating that the fresh soot particles aged during

295   the dust storm movement from the inland to the coastal area. Meanwhile, we found that

296   the D_f value at T1 changed from 1.65 at T1 to 1.84 at T2. The strong diffusion during

297   the dust storm is not conducive to soot accumulation (Pan et al., 2015). Although local

298   emissions at T2 could interference the observation of soot aging process, long-range

299   transported soot particles were still dominant at T2 during the cold front. These results

300   indicate that the morphological structures of soot particles underwent changes along

301   with the dust storm movement. In a word, large amounts of fresh soot converted into

302   partially embedded soot particles from T1 to T2 (Figure 4).

303   Figure 4 shows that the fresh soot particles disappeared at T3, and the number

304   fraction of fully embedded soot particles increased to 84%. Moreover, the D_f of soot

305   particles had a large change from 1.84 at T2 to 1.91 at T3, which suggests that the

306   morphology structure of soot particles changed from chain-like to compact when the

307   air masses crossed the East China Sea (Figure 5).

308   Secondary aerosol formation on soot particles can significantly change their fractal

309   morphology into a compact shape (China et al., 2015;Wang et al., 2017;Ma et al.,

310   2013;Pei et al., 2018). The thick coating of soot particles occurred when air masses

311   crossed the East China Sea (Figure 6b), suggesting that secondary aerosol coating

312   formation can significantly compress the fractal morphology of soot particles. Recently,

313   Yuan et al. (2019) further found that the phase change of secondary aerosols (due to RH

314   variation) in aged soot particles could further compress the fractal shape of soot

315   aggregates. The high humidity in marine air (T2 to T3) should lead to phase changes of

316   secondary aerosols and further cause the morphological compactness of soot

317   aggregations. These two reasons are able to explain the change in soot fractal dimension

318   from T2 to T3 (Figure 5).

319   TEM observations present a particular mixing structure of the fully embedded soot

320   at T3: organic coating instead of sulfate contains several typical soot particles, and the

321   organic coating spreads on the substrate (named droplet-like particles (O'Brien et al.,

322   2015;Li et al., 2011)) (Figures 3d and 7c). More than half of this type of particles

323   contain one or two soot fragments, while 43% of them include more than three soot

324   fragments (Figure S7). The droplet-like coating morphology of soot can reflect that

325   these secondary particles were in an aqueous phase at T3 in the air. Similar droplet-like

326   particles were not observed at T1 and T2 (Figure 7a and b). A previous study has shown

327   that secondary aerosol particles begin to acquire aqueous shells at RH 60% (Sun et al.,

328   2018). Once secondary aerosols change from a solid to liquid phase following an RH

329   increase in marine air, soot particles tend to adhere to the liquid phase through

330   coagulation (Li et al., 2016b). Figure 7c shows the phase separation of the organic

331   coating and sulfate core on the substrate under the phenomenon of liquid-liquid phase

332   separations (You et al., 2012). Recently, Brunamonti et al. (2015) found that soot

333   particles tend to redistribute into the organic coating during liquid-liquid phase

334   separation. Therefore, the soot distribution in the organic coating indicates that aerosol

335   particles in the air mass at T3 underwent an aqueous aging process over the East China

336   Sea, which is different from the continental aerosol particles at T1 and T2. It must be

337   noted that several tiny soot particles were distributed in the organic coating at T3

338   (Figure 7c), which did not occur at T1 and T2. There is no previous study to report the

339   tiny scattered soot in the organic coating. We proposed a possible reason that soot

340   particle with smaller size have a longer lifetime and could be transported over longer

341   distances. Therefore, the tiny soot particles have more chances to coagulate with

342   preexisting aqueous secondary particles in marine air (Liu et al., 2018). Our findings

343   suggest that the complex aqueous process of individual particles in marine air could

344 result in scattered soot particles, but further studies are required to reveal the detailed

345 reasons.

346   Tracing the soot particles during the dust storm, we can clarify that the morphology

347 change of soot particles depends on the secondary coating thickness and relative

348 humidity in the air. The microscopic changes between soot and coating could change

349 their optical absorption, which is different from the core-shell absorption (He et al.,

350 2015). Our study proposes that BC-related optical models should not only consider the

351 mixing state of soot particles but also incorporate the morphological structure of soot

352 particles in different environmental air.

353   Based on the results and discussion above, we propose a conceptual model to

354 summarize the evolution of morphology and mixing state of soot particles along with

355 the movement of an Asian dust storm (Figure 8). Dust storms in East Asia could carry

356 soot and other anthropogenic pollutants from urban areas to downwind areas. During

357 the transport, the dominated mixing structure of individual soot particles changed from

358 fresh to partially embedded and finally to fully embedded. Meanwhile, the chain-like

359 soot compressed and had a rounder shape depending on secondary coating thickness

360 and relative humidity.

361 **4. Conclusions**

362   Individual aerosol particles were collected from 18 to 19 March 2014 during an

363 Asian dust storm event. Three sampling sites along with the pathway of the dust storm

364 were chosen to study soot aging, including an inland urban site in Jinan city, China (T1),

365 a coastal urban site in Qingdao city, China (T2), and a coastal rural site at Amakusa in

366 southwestern Japan (T3). Soot-bearing particles were classified into three types: fresh,

367 partially embedded, and fully embedded. There was a noticeable difference in the

368   mixing structure of soot particles during long-range transport, with 71% fresh soot in

369   the analyzed soot particles (by number) at T1, 68% partially embedded soot at T2, and

370   84% fully embedded soot at T3. The fractal dimension (D_f) of soot particles at T3 (1.91)

371   was higher than that at the other two sites (1.65 and 1.84), suggesting that soot particles

372   converted from chain-like to compact shapes during long-range transport. This study

373   showed that an increasing number of soot particles were internally mixed with

374   secondary aerosol particles and significantly aged during transport. The average ratio

375   of D_p/D_{core} during the dust storm period was 1.42 at T1, 1.78 at T2, and 2.49 at T3,

376   indicating increasing coating thickness. By comparing the soot fractal dimension in

377   continental air and marine air, we found that secondary coating thickness and relative

378   humidity both can significantly change the fractal morphology of soot particles in the

379   air. Individual particle analysis showed that several tiny soot particles only observed in

380   organic coatings instead of sulfate in individual soot-bearing particles at T3.

381

382   **Data availability**

383   All data presented in this paper are available upon request from the corresponding

384   author (liweijun@zju.edu.cn).

385   **Supporting information**

386   Table S1 and Figures S1-S9

387   **Author contributions**

388   LX and WL conceived the study and wrote the manuscript. The field campaign was

389   organized and supervised by WL and DZ. SF, KM, AN, and TK collected aerosol

390 particles. LX, SS, LL, YW, HN, and ZS contributed sample and data analyses. All

391 authors reviewed and commented on the paper.

392 **Competing interests**

393 The authors declare that they have no conflict of interest.

399

400 **References**

401 Adachi, K., Moteki, N., Kondo, Y., and Igarashi, Y.: Mixing states of light-absorbing particles measured
402   using a transmission electron microscope and a single-particle soot photometer in Tokyo, Japan, J.
403   Geophys. Res.: Atmos., 121, 9153-9164, https://doi.org/10.1002/2016JD025153, 2016.

404 Bond, T. C., Doherty, S. J., Fahey, D. W., Forster, P. M., Berntsen, T., DeAngelo, B. J., Flanner, M. G.,
405   Ghan, S., Kärcher, B., Koch, D., Kinne, S., Kondo, Y., Quinn, P. K., Sarofim, M. C., Schultz, M. G.,
406   Schulz, M., Venkataraman, C., Zhang, H., Zhang, S., Bellouin, N., Guttikunda, S. K., Hopke, P. K.,
407   Jacobson, M. Z., Kaiser, J. W., Klimont, Z., Lohmann, U., Schwarz, J. P., Shindell, D., Storelvmo, T.,
408   Warren, S. G., and Zender, C. S.: Bounding the role of black carbon in the climate system: A scientific
409   assessment, J. Geophys. Res.: Atmos., 118, 5380-5552, https://doi.org/10.1002/jgrd.50171, 2013.

410 Brasil, A. M., Farias, T. L., and Carvalho, M. G.: A recipe for image characterization of fractal-Like
411   aggregates, J. Aerosol Sci, 30, 1379-1389, https://doi.org/10.1016/S0021-8502(99)00026-9, 1999.

412 Brunamonti, S., Krieger, U. K., Marcolli, C., and Peter, T.: Redistribution of black carbon in aerosol
413   particles undergoing liquid－liquid phase separation, Geophys. Res. Lett., 42, 2532-2539,
414   https://doi.org/10.1002/2014GL062908, 2015.

415 Buseck, P. R., Adachi, K., Gelencsér, A., Tompa, É., and Pósfai, M.: Ns-Soot: A Material-Based Term for
416   Strongly Light-Absorbing Carbonaceous Particles, Aerosol Sci. Technol., 48, 777-788,
417   https://doi.org/10.1080/02786826.2014.919374, 2014.

418 Cappa, C. D., Onasch, T. B., Massoli, P., Worsnop, D. R., Bates, T. S., Cross, E. S., Davidovits, P., Hakala,
419   J., Hayden, K. L., Jobson, B. T., Kolesar, K. R., Lack, D. A., Lerner, B. M., Li, S.-M., Mellon, D.,
420   Nuaaman, I., Olfert, J. S., Petäjä, T., Quinn, P. K., Song, C., Subramanian, R., Williams, E. J., and
421   Zaveri, R. A.: Radiative Absorption Enhancements Due to the Mixing State of Atmospheric Black
422   Carbon, Science, 337, 1078-1081, https://doi.org/10.1126/science.1223447, 2012.

423 Chakrabarty, R. K., Moosmüller, H., Garro, M. A., Arnott, W. P., Walker, J., Susott, R. A., Babbitt, R. E.,
424   Wold, C. E., Lincoln, E. N., and Hao, W. M.: Emissions from the laboratory combustion of wildland

425 fuels: Particle morphology and size, J. Geophys. Res.: Atmos., 111,
426 https://doi.org/10.1029/2005JD006659, 2006.

427 Chi, J. W., Li, W. J., Zhang, D. Z., Zhang, J. C., Lin, Y. T., Shen, X. J., Sun, J. Y., Chen, J. M., Zhang, X.
428 Y., Zhang, Y. M., and Wang, W. X.: Sea salt aerosols as a reactive surface for inorganic and organic
429 acidic gases in the Arctic troposphere, Atmos. Chem. Phys., 15, 11341-11353,
430 https://doi.org/10.5194/acp-15-11341-2015, 2015.

431 China, S., Mazzoleni, C., Gorkowski, K., Aiken, A. C., and Dubey, M. K.: Morphology and mixing state
432 of individual freshly emitted wildfire carbonaceous particles, Nat. Commun., 4, 2122,
433 https://doi.org/10.1038/ncomms3122, 2013.

434 China, S., Scarnato, B., Owen, R. C., Zhang, B., Ampadu, M. T., Kumar, S., Dzepina, K., Dziobak, M.
435 P., Fialho, P., and Perlinger, J. A.: Morphology and mixing state of aged soot particles at a remote
436 marine free troposphere site: Implications for optical properties, Geophys. Res. Lett., 42, 1243-1250,
437 https://doi.org/10.1002/2014GL062404, 2015.

438 Dahlkötter, F., Gysel, M., Sauer, D., Minikin, A., Baumann, R., Seifert, P., Ansmann, A., Fromm, M.,
439 Voigt, C., and Weinzierl, B.: The Pagami Creek smoke plume after long-range transport to the upper
440 troposphere over Europe – aerosol properties and black carbon mixing state, Atmos. Chem.
441 Phys., 14, 6111-6137, https://doi.org/10.5194/acp-14-6111-2014, 2014.

442 Ding, A. J., Huang, X., Nie, W., Sun, J. N., Kerminen, V. M., Petäjä, T., Su, H., Cheng, Y. F., Yang, X.
443 Q., Wang, M. H., Chi, X. G., Wang, J. P., Virkkula, A., Guo, W. D., Yuan, J., Wang, S. Y., Zhang, R.
444 J., Wu, Y. F., Song, Y., Zhu, T., Zilitinkevich, S., Kulmala, M., and Fu, C. B.: Enhanced haze pollution
445 by black carbon in megacities in China, Geophys. Res. Lett., 43, 2873-2879,
446 https://doi.org/10.1002/2016GL067745, 2016.

447 Ding, S., Liu, D., Zhao, D., Hu, K., Tian, P., Zhou, W., Huang, M., Yang, Y., Wang, F., Sheng, J., Liu, Q.,
448 Kong, S., Cui, P., Huang, Y., He, H., Coe, H., and Ding, D.: Size-Related Physical Properties of Black
449 Carbon in the Lower Atmosphere over Beijing and Europe, Environ. Sci. Technol., 53, 11112-11121,
450 https://doi.org/10.1021/acs.est.9b03722, 2019.

451 Geng, H., Hwang, H., Liu, X., Dong, S., and Ro, C. U.: Investigation of aged aerosols in size-resolved
452 Asian dust storm particles transported from Beijing, China, to Incheon, Korea, using low-Z particle
453 EPMA, Atmos. Chem. Phys., 14, 3307-3323, https://doi.org/10.5194/acp-14-3307-2014, 2014.

454 He, C., Liou, K. N., Takano, Y., Zhang, R., Levy Zamora, M., Yang, P., Li, Q., and Leung, L. R.: Variation
455 of the radiative properties during black carbon aging: theoretical and experimental intercomparison,
456 Atmos. Chem. Phys., 15, 11967-11980, https://doi.org/10.5194/acp-15-11967-2015, 2015.

457 Healy, R. M., Riemer, N., Wenger, J. C., Murphy, M., West, M., Poulain, L., Wiedensohler, A., O'Connor,
458 I. P., McGillicuddy, E., Sodeau, J. R., and Evans, G. J.: Single particle diversity and mixing state
459 measurements, Atmos. Chem. Phys., 14, 6289-6299, https://doi.org/10.5194/acp-14-6289-2014, 2014.

460 IPCC.: Clouds and Aerosols. In: Climate Change 2013: The Physical Science Basis, Contribution of
461 Working Group I to the Fifth Assessment Report of the Intergovernmental Panel on Climate Change.
462 Intergovernmental Panel on Climate Change (IPCC), 571- 657, 2013.

463 Jacobson, M. Z.: Strong radiative heating due to the mixing state of black carbon in atmospheric aerosols,
464 Nature, 409, 695-697, https://doi.org/10.1038/35055518, 2001.

465 Koeylue, U., Xing, Y., and Rosner, D. E.: Fractal Morphology Analysis of Combustion-Generated
466 Aggregates Using Angular Light Scattering and Electron Microscope Images, Langmuir, 11, 4848-
467 4854, https://doi.org/10.1021/la00012a043, 1995.

468 Laskin, A., Moffet, R. C., and Gilles, M. K.: Chemical Imaging of Atmospheric Particles, Acc. Chem.

Res., 52, 3419-3431, https://doi.org/10.1021/acs.accounts.9b00396, 2019.

Lee, A. K. Y., Rivellini, L.-H., Chen, C.-L., Liu, J., Price, D. J., Betha, R., Russell, L. M., Zhang, X., and Cappa, C. D.: Influences of Primary Emission and Secondary Coating Formation on the Particle Diversity and Mixing State of Black Carbon Particles, Environ. Sci. Technol., 53, 9429-9438, https://doi.org/10.1021/acs.est.9b03064, 2019.

Li, J., Liu, C., Yin, Y., and Kumar, K. R.: Numerical investigation on the Ångström exponent of black carbon aerosol, J. Geophys. Res.: Atmos., 121, 3506-3518, https://doi.org/10.1002/2015JD024718, 2016a.

Li, W., Zhou, S., Wang, X., Xu, Z., Yuan, C., Yu, Y., Zhang, Q., and Wang, W.: Integrated evaluation of aerosols from regional brown hazes over northern China in winter: Concentrations, sources, transformation, and mixing states, J. Geophys. Res.: Atmos., 116, D09301, https://doi.org/10.1029/2010JD015099, 2011.

Li, W., Shao, L., Shi, Z., Chen, J., Yang, L., Yuan, Q., Yan, C., Zhang, X., Wang, Y., Sun, J., Zhang, Y., Shen, X., Wang, Z., and Wang, W.: Mixing state and hygroscopicity of dust and haze particles before leaving Asian continent, J. Geophys. Res.: Atmos., 119, 1044-1059, https://doi.org/10.1002/2013JD021003, 2014.

Li, W., Sun, J., Xu, L., Shi, Z., Riemer, N., Sun, Y., Fu, P., Zhang, J., Lin, Y., Wang, X., Shao, L., Chen, J., Zhang, X., Wang, Z., and Wang, W.: A conceptual framework for mixing structures in individual aerosol particles, J. Geophys. Res.: Atmos., 121, 13784-13798, https://doi.org/10.1002/2016JD025252, 2016b.

Liu, D., Whitehead, J., Alfarra, M. R., Reyes-Villegas, E., Spracklen, D. V., Reddington, C. L., Kong, S., Williams, P. I., Ting, Y.-C., Haslett, S., Taylor, J. W., Flynn, M. J., Morgan, W. T., McFiggans, G., Coe, H., and Allan, J. D.: Black-carbon absorption enhancement in the atmosphere determined by particle mixing state, Nat. Geosci., 10, 184-188, https://doi.org/10.1038/ngeo2901, 2017.

Liu, L., Zhang, J., Xu, L., Yuan, Q., Huang, D., Chen, J., Shi, Z., Sun, Y., Fu, P., Wang, Z., Zhang, D., and Li, W.: Cloud scavenging of anthropogenic refractory particles at a mountain site in North China, Atmos. Chem. Phys., 18, 14681-14693, https://doi.org/10.5194/acp-18-14681-2018, 2018.

Ma, X., Zangmeister, C. D., Gigault, J., Mulholland, G. W., and Zachariah, M. R.: Soot aggregate restructuring during water processing, J. Aerosol Sci, 66, 209-219, https://doi.org/10.1016/j.jaerosci.2013.08.001, 2013.

Matsui, H., Hamilton, D. S., and Mahowald, N. M.: Black carbon radiative effects highly sensitive to emitted particle size when resolving mixing-state diversity, Nat. Commun., 9, 3446, https://doi.org/10.1038/s41467-018-05635-1, 2018.

Metcalf, A. R., Craven, J. S., Ensberg, J. J., Brioude, J., Angevine, W., Sorooshian, A., Duong, H. T., Jonsson, H. H., Flagan, R. C., and Seinfeld, J. H.: Black carbon aerosol over the Los Angeles Basin during CalNex, J. Geophys. Res.: Atmos., 117, D00V13, https://doi.org/10.1029/2011JD017255, 2012.

Moffet, R. C., and Prather, K. A.: In-situ measurements of the mixing state and optical properties of soot with implications for radiative forcing estimates, Proc. Natl. Acad. Sci. U.S.A., 106, 11872-11877, https://doi.org/10.1073/pnas.0900040106, 2009.

O'Brien, R. E., Wang, B., Kelly, S. T., Lundt, N., You, Y., Bertram, A. K., Leone, S. R., Laskin, A., and Gilles, M. K.: Liquid–Liquid Phase Separation in Aerosol Particles: Imaging at the Nanometer Scale, Environ. Sci. Technol., 49, 4995-5002, https://doi.org/10.1021/acs.est.5b00062, 2015.

Oh, C., and Sorensen, C. M.: The Effect of Overlap between Monomers on the Determination of Fractal

513   Cluster Morphology, J. Colloid Interface Sci., 193, 17-25, https://doi.org/10.1006/jcis.1997.5046,
514   1997.

515   Pan, X., Uno, I., Hara, Y., Kuribayashi, M., Kobayashi, H., Sugimoto, N., Yamamoto, S., Shimohara, T.,
516   and Wang, Z.: Observation of the simultaneous transport of Asian mineral dust aerosols with
517   anthropogenic pollutants using a POPC during a long-lasting dust event in late spring 2014, Geophys.
518   Res. Lett., 42, 1593-1598, https://doi.org/10.1002/2014GL062491, 2015.

519   Pei, X., Hallquist, M., Eriksson, A. C., Pagels, J., Donahue, N. M., Mentel, T., Svenningsson, B., Brune,
520   W., and Pathak, R. K.: Morphological transformation of soot: investigation of microphysical
521   processes during the condensation of sulfuric acid and limonene ozonolysis product vapors, Atmos.
522   Chem. Phys., 18, 9845-9860, https://doi.org/10.5194/acp-18-9845-2018, 2018.

523   Peng, J., Hu, M., Guo, S., Du, Z., Shang, D., Zheng, J., Zheng, J., Zeng, L., Shao, M., Wu, Y., Collins,
524   D., and Zhang, R.: Ageing and hygroscopicity variation of black carbon particles in Beijing measured
525   by a quasi-atmospheric aerosol evolution study (QUALITY) chamber, Atmos. Chem. Phys., 17,
526   10333-10348, https://doi.org/10.5194/acp-17-10333-2017, 2017.

527   Perring, A. E., Schwarz, J. P., Markovic, M. Z., Fahey, D. W., Jimenez, J. L., Campuzano-Jost, P., Palm,
528   B. D., Wisthaler, A., Mikoviny, T., Diskin, G., Sachse, G., Ziemba, L., Anderson, B., Shingler, T.,
529   Crosbie, E., Sorooshian, A., Yokelson, R., and Gao, R.-S.: In situ measurements of water uptake by
530   black carbon-containing aerosol in wildfire plumes, J. Geophys. Res.: Atmos., 122, 1086-1097,
531   https://doi.org/10.1002/2016JD025688, 2017.

532   Raatikainen, T., Brus, D., Hyvärinen, A. P., Svensson, J., Asmi, E., and Lihavainen, H.: Black carbon
533   concentrations and mixing state in the Finnish Arctic, Atmos. Chem. Phys., 15, 10057-10070,
534   https://doi.org/10.5194/acp-15-10057-2015, 2015.

535   Riemer, N., West, M., Zaveri, R., and Easter, R.: Estimating black carbon aging time-scales with a
536   particle-resolved   aerosol   model,   J.   Aerosol   Sci,   41,   143-158,
537   https://doi.org/10.1016/j.jaerosci.2009.08.009, 2010.

538   Riemer, N., and West, M.: Quantifying aerosol mixing state with entropy and diversity measures, Atmos.
539   Chem. Phys., 13, 11423-11439, https://doi.org/10.5194/acp-13-11423-2013, 2013.

540   Sahu, L. K., Kondo, Y., Moteki, N., Takegawa, N., Zhao, Y., Cubison, M. J., Jimenez, J. L., Vay, S.,
541   Diskin, G. S., Wisthaler, A., Mikoviny, T., Huey, L. G., Weinheimer, A. J., and Knapp, D. J.: Emission
542   characteristics of black carbon in anthropogenic and biomass burning plumes over California during
543   ARCTAS-CARB   2008,   J.   Geophys.   Res.:   Atmos.,   117,   D16302,
544   https://doi.org/10.1029/2011JD017401, 2012.

545   Shiraiwa, M., Kondo, Y., Moteki, N., Takegawa, N., Miyazaki, Y., and Blake, D. R.: Evolution of mixing
546   state of black carbon in polluted air from Tokyo, Geophys. Res. Lett., 34, L16803,
547   https://doi.org/10.1029/2007GL029819, 2007.

548   Stein, A. F., Draxler, R. R., Rolph, G. D., Stunder, B. J. B., Cohen, M. D., and Ngan, F.: NOAA's
549   HYSPLIT Atmospheric Transport and Dispersion Modeling System, Bull. Amer. Meteor. Soc., 96,
550   2059-2077, https://doi.org/10.1175/bams-d-14-00110.1, 2015.

551   Sun, J., Liu, L., Xu, L., Wang, Y., Wu, Z., Hu, M., Shi, Z., Li, Y., Zhang, X., Chen, J., and Li, W.: Key
552   Role of Nitrate in Phase Transitions of Urban Particles: Implications of Important Reactive Surfaces
553   for   Secondary   Aerosol   Formation,   J.   Geophys.   Res.:   Atmos.,   123,   1234-1243,
554   https://doi.org/10.1002/2017JD027264, 2018.

555   Ueda, S., Nakayama, T., Taketani, F., Adachi, K., Matsuki, A., Iwamoto, Y., Sadanaga, Y., and Matsumi,
556   Y.: Light absorption and morphological properties of soot-containing aerosols observed at an East

557   Asian outflow site, Noto Peninsula, Japan, Atmos. Chem. Phys., 16, 2525-2541,
558   https://doi.org/10.5194/acp-16-2525-2016, 2016.

559 Wang, J., Cubison, M. J., Aiken, A. C., Jimenez, J. L., and Collins, D. R.: The importance of aerosol
560   mixing state and size-resolved composition on CCN concentration and the variation of the importance
561   with atmospheric aging of aerosols, Atmos. Chem. Phys., 10, 7267-7283, https://doi.org/10.5194/acp-
562   10-7267-2010, 2010.

563 Wang, Y., Liu, F., He, C., Bi, L., Cheng, T., Wang, Z., Zhang, H., Zhang, X., Shi, Z., and Li, W.: Fractal
564   Dimensions and Mixing Structures of Soot Particles during Atmospheric Processing, Environ. Sci.
565   Technol. Lett., 4, 487-493, https://doi.org/10.1021/acs.estlett.7b00418, 2017.

566 Wentzel, M., Gorzawski, H., Naumann, K. H., Saathoff, H., and Weinbruch, S.: Transmission electron
567   microscopical and aerosol dynamical characterization of soot aerosols, J. Aerosol Sci, 34, 1347-1370,
568   https://doi.org/10.1016/S0021-8502(03)00360-4, 2003.

569 West, J. J., Cohen, A., Dentener, F., Brunekreef, B., Zhu, T., Armstrong, B., Bell, M. L., Brauer, M.,
570   Carmichael, G., Costa, D. L., Dockery, D. W., Kleeman, M., Krzyzanowski, M., Künzli, N., Liousse,
571   C., Lung, S.-C. C., Martin, R. V., Pöschl, U., Pope, C. A., Roberts, J. M., Russell, A. G., and
572   Wiedinmyer, C.: "What We Breathe Impacts Our Health: Improving Understanding of the Link
573   between Air Pollution and Health", Environ. Sci. Technol., 50, 4895-4904,
574   https://doi.org/10.1021/acs.est.5b03827, 2016.

575 Wu, Y., Cheng, T., Liu, D., Allan, J. D., Zheng, L., and Chen, H.: Light Absorption Enhancement of Black
576   Carbon Aerosol Constrained by Particle Morphology, Environ. Sci. Technol., 52, 6912-6919,
577   https://doi.org/10.1021/acs.est.8b00636, 2018.

578 Xu, L., Zhang, D., and Li, W.: Microscopic comparison of aerosol particles collected at an urban site in
579   North China and a coastal site in Japan, Sci. Total Environ., 669, 948-954,
580   https://doi.org/10.1016/j.scitotenv.2019.03.163, 2019.

581 You, Y., Renbaum-Wolff, L., Carreras-Sospedra, M., Hanna, S. J., Hiranuma, N., Kamal, S., Smith, M.
582   L., Zhang, X., Weber, R. J., Shilling, J. E., Dabdub, D., Martin, S. T., and Bertram, A. K.: Images
583   reveal that atmospheric particles can undergo liquid–liquid phase separations, Proc. Natl. Acad. Sci.
584   U.S.A., 109, 13188-13193, https://doi.org/10.1073/pnas.1206414109, 2012.

585 Yuan, Q., Xu, J., Wang, Y., Zhang, X., Pang, Y., Liu, L., Bi, L., Kang, S., and Li, W.: Mixing State and
586   Fractal Dimension of Soot Particles at a Remote Site in the Southeastern Tibetan Plateau, Environ.
587   Sci. Technol., 53, 8227-8234, https://doi.org/10.1021/acs.est.9b01917, 2019.

588 Zhang, D., Iwasaka, Y., Shi, G., Zang, J., Hu, M., and Li, C.: Separated status of the natural dust plume
589   and polluted air masses in an Asian dust storm event at coastal areas of China, J. Geophys. Res.:
590   Atmos., 110, D06302, https://doi.org/10.1029/2004JD005305, 2005.

591 Zhang, G., Bi, X., Li, L., Chan, L. Y., Li, M., Wang, X., Sheng, G., Fu, J., and Zhou, Z.: Mixing state of
592   individual submicron carbon-containing particles during spring and fall seasons in urban Guangzhou,
593   China: a case study, Atmos. Chem. Phys., 13, 4723-4735, https://doi.org/10.5194/acp-13-4723-2013,
594   2013.

595 Zhang, R., Khalizov, A. F., Pagels, J., Zhang, D., Xue, H., and McMurry, P. H.: Variability in morphology,
596   hygroscopicity, and optical properties of soot aerosols during atmospheric processing, Proc. Natl.
597   Acad. Sci. U.S.A., 105, 10291-10296, https://doi.org/10.1073/pnas.0804860105, 2008.

598 Zhang, X., Mao, M., Yin, Y., and Wang, B.: Numerical Investigation on Absorption Enhancement of
599   Black Carbon Aerosols Partially Coated With Nonabsorbing Organics, J. Geophys. Res.: Atmos., 123,
600   1297-1308, https://doi.org/10.1002/2017JD027833, 2018a.

601 Zhang, Y., Su, H., Ma, N., Li, G., Kecorius, S., Wang, Z., Hu, M., Zhu, T., He, K., Wiedensohler, A.,
602   Zhang, Q., and Cheng, Y.: Sizing of Ambient Particles From a Single-Particle Soot Photometer
603   Measurement to Retrieve Mixing State of Black Carbon at a Regional Site of the North China Plain,
604   J. Geophys. Res.: Atmos., 123, 12,778-712,795, https://doi.org/10.1029/2018JD028810, 2018b.

605
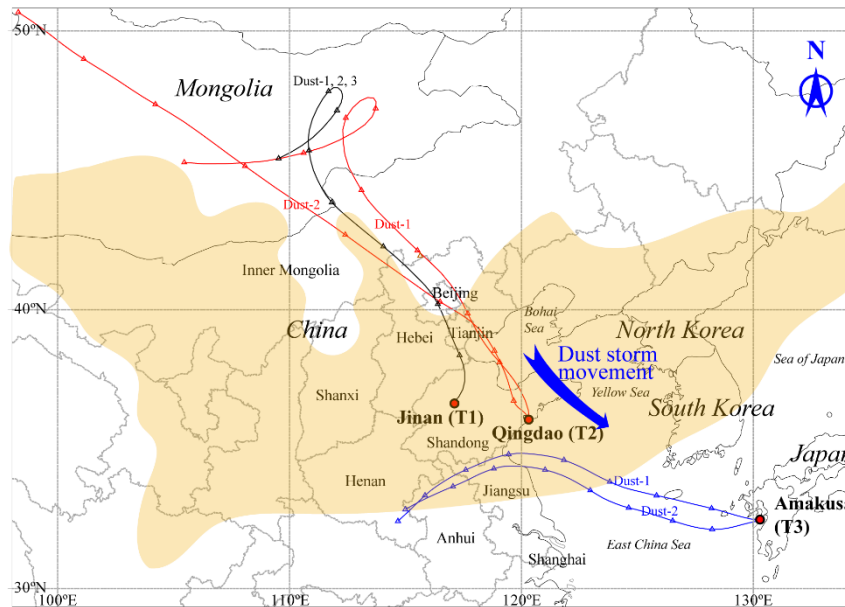
Figure 1. The locations of the three sampling sites and HYSPLIT forty-eight hour air mass backward trajectories arriving at 1500 m above ground level at T1, T2, and T3 sites. The interval between two triangle symbols is six hours. The yellow shadow is derived from Figure S1, which represents the area influenced by the dust storm at 00:00 on 2014/03/18 (UTC).
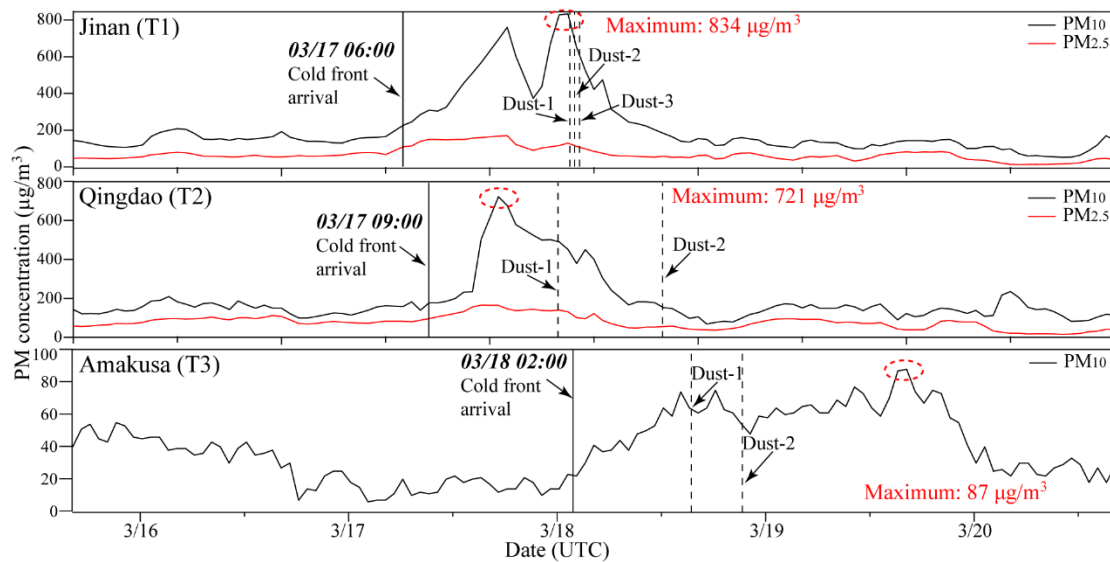
Figure 2. Time series of PM (particulate matter) concentrations at T1, T2, and T3 during sampling. The cold front arrival times indicate the time when the sampling site starts to be influenced by the dust storm. Data sources: T1 and T2: The Ministry of Ecology and Environment of the People's Republic of China, https://www.aqistudy.cn/; T3: National Institute for Environmental Studies of Japan, https://www.nies.go.jp/igreen/).
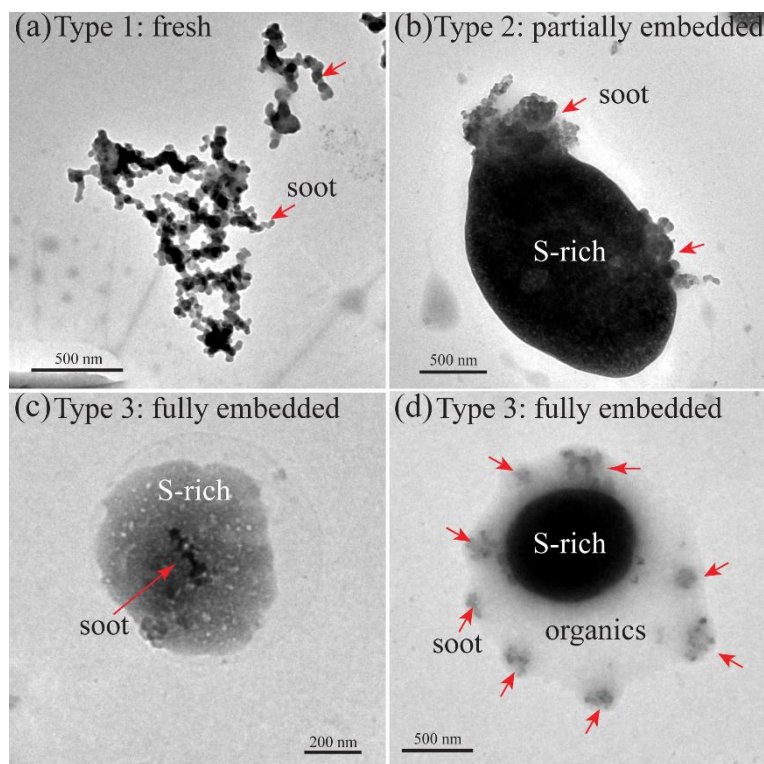
Figure 3. Morphology of soot-bearing aerosol particles: (a) fresh chain-like soot aggregates with no visible coating; (b) partially embedded soot: part of the soot particle was coated by secondary aerosols; (c) fully embedded soot: the whole soot particle was encapsulated by secondary aerosols; (d) a subtype of fully embedded soot: individual soot particles were only embedded in the organic coating on a sulfur-rich particle.
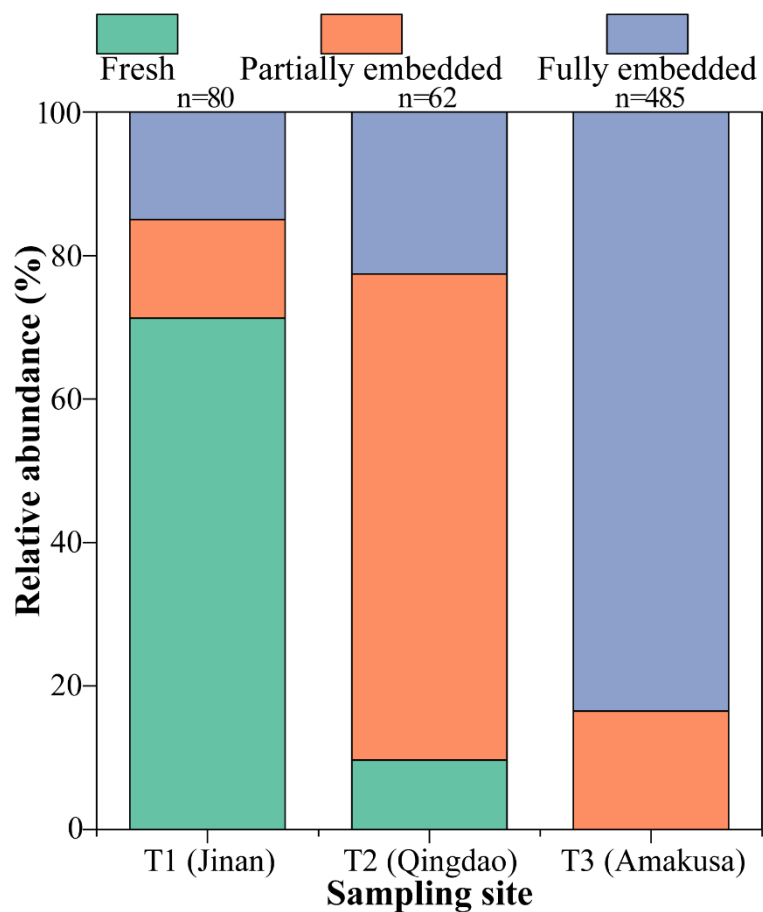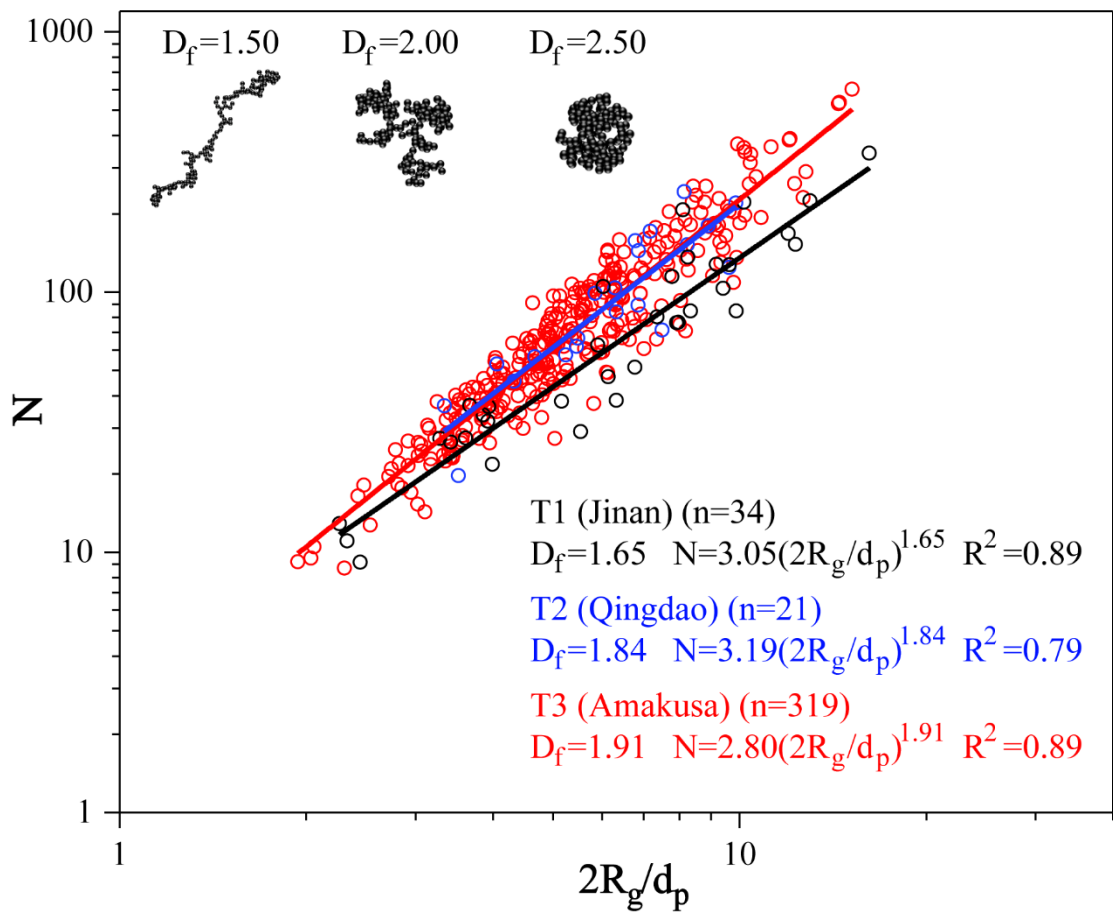
Figure 4. Relative abundance of three types of soot-bearing aerosol particles at the three sampling sites. The number of analyzed soot-bearing particles is shown above the column.

Figure 5. Fractal dimension of soot-bearing particles at the three sampling sites. The parameter n in parentheses represents the total number of soot particles analyzed for each site to calculate D_f and k_g. Three model simulated soot particles with different D_f are presented to represent different soot morphology. The inconsistency of analyzed soot number in Figure 4 and 5 is attributed to the indistinct soot particles in the low-magnification TEM images that can be identified as soot but cannot provide necessary data for D_f analysis.
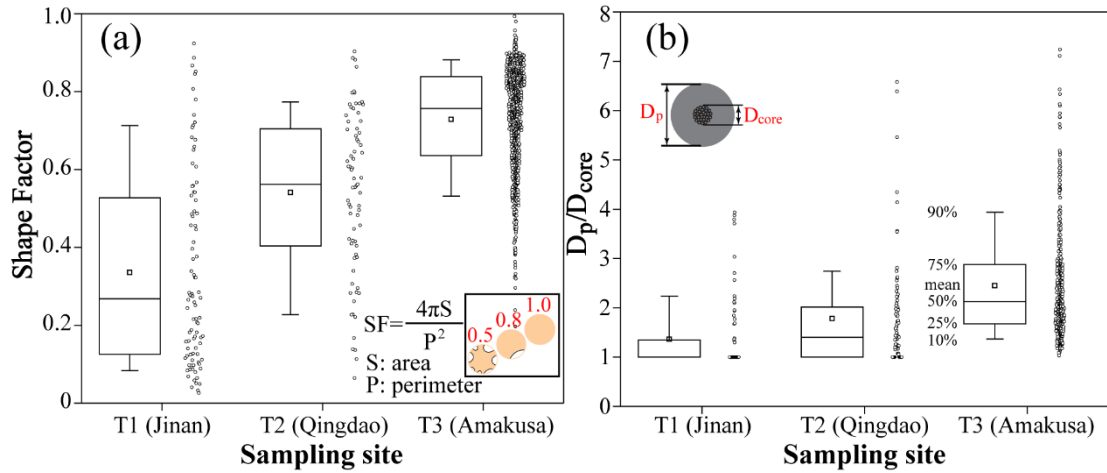
Figure 6. (a) Shape factor of soot-bearing particles and (b) the particle-to-soot core diameter ratio (D_p/D_{core}) at the three sampling sites.
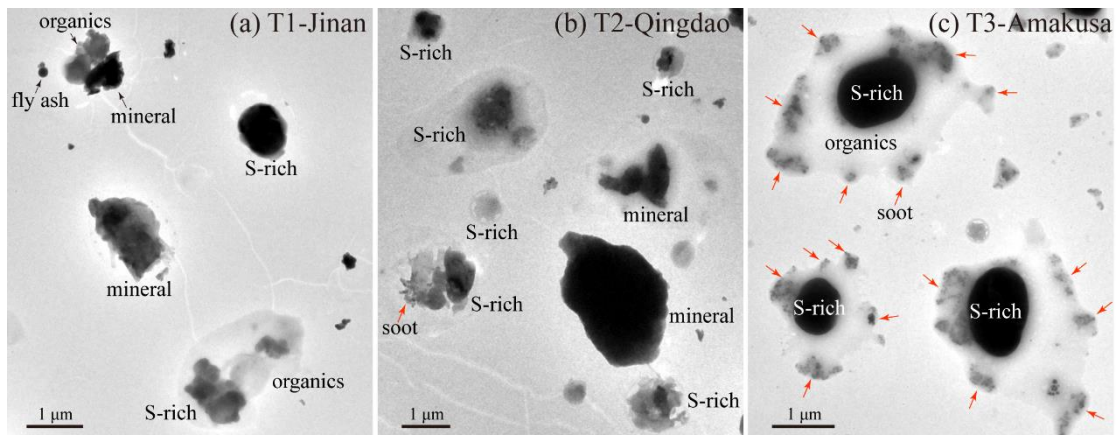
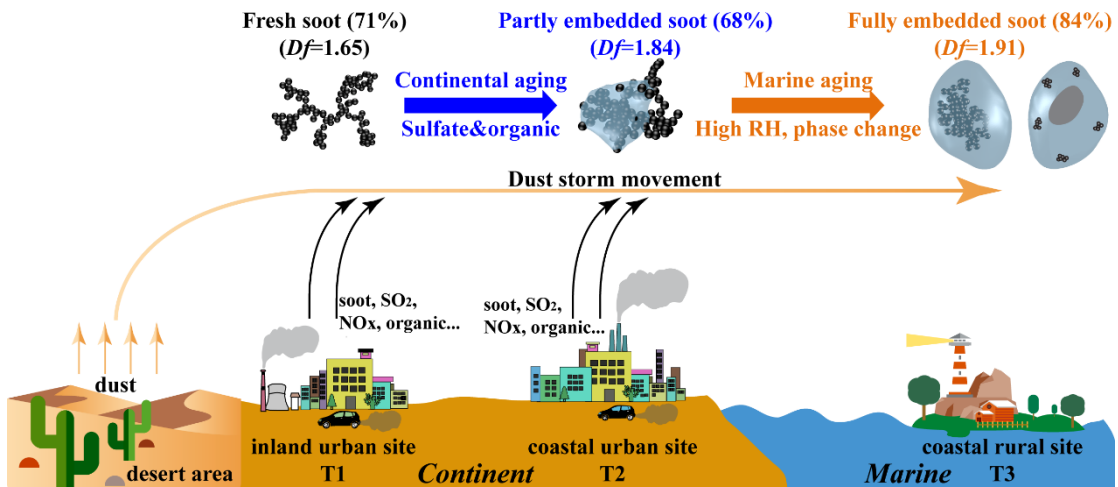Figure 7. Low-magnification TEM images at T1, T2, and T3.

Figure 8. Schematic diagram showing the evolution of morphology and mixing state of

648   soot particles along with the movement of an Asian dust storm